


Can the double-slit experiment distinguish between quantum interpretations?

Ali Ayatollah Rafsanjani ^{1,2}, MohammadJavad Kazemi ³, Alireza Bahrampour^{1,4} & Mehdi Golshani^{2,4}

Despite the astonishing successes of quantum mechanics, due to some fundamental problems such as the measurement problem and quantum arrival time problem, the predictions of the theory are in some cases not quite clear and unique. Especially, there are various predictions for the joint spatiotemporal distribution of particle detection events on a screen, which are derived from different formulations and interpretations of the quantum theory. Although the differences are typically small, we show that these predictions can be experimentally distinguished by a proposed unconventional double-slit configuration, which is realizable using present-day single-atom interferometry. This experiment would enrich our understanding of the foundations of quantum mechanics.

¹ Department of Physics, Sharif University of Technology, Tehran, Iran. ² School of Physics, Institute for Research in Fundamental Sciences (IPM), Tehran, Iran. ³ Department of Physics, Faculty of Science, University of Qom, Qom, Iran. ⁴ These authors jointly supervised this work: Alireza Bahrampour, Mehdi Golshani. email: aliayat@physics.sharif.edu

In textbook quantum theory, time is a parameter, not a self-adjoint operator¹, hence there is no agreed-upon way to compute the temporal probability distribution of events from the first principles (i.e. the Born rule). Nonetheless, since clocks exist and time measurements are routinely performed in quantum experiments^{2,3}, a complete quantum theory must be able to predict the temporal statistics of detection events. For example, in the famous double slit experiment, each particle is detected at a random time as same as at a random *position* on the detection screen^{4–9}. Therefore, one can ask: What is the position-time joint probability density $\mathbb{P}(\mathbf{x}, t)$ on the screen? Although this question is very old^{10–14}, it is still open^{15–21}. In fact, the ambiguity in the arrival time distribution even prevents a clear prediction of cumulative arrival position distribution, $\int \mathbb{P}(\mathbf{x}, t) dt$, which is typically measured in a non-time-resolved double-slit experiment. Note that, the Heisenberg position operator describes position measurement at a specific time, not position measurements at random times^{22,23}. In other words, $|\psi_t(\mathbf{x})|^2$ is just the *conditional* position probability density at the specific time $\mathbb{P}(\mathbf{x}|t)$ ^{16,17,24,25}, not the position-time joint probability density^{9,26,27}.

Nonetheless, usual experiments are performed in the far-field (or scattering) regime, where a semiclassical analysis is often sufficient¹⁵. In this analysis, it is assumed that particles move along classical trajectories, and the arrival time distribution is computed using the quantum momentum distribution^{8,28,29}. However, because of the *quantum backflow* effect³⁰, even in free space, the quantum mechanical time evolution of position probability density is not consistent with the underlying uniform motion assumption, especially in near-field interference phenomena³¹. In fact, due to recent progress in ultra-fast detector technology^{32–35}, it will soon be possible to investigate the near-field regime, where the semiclassical approximation breaks down and a deeper analysis is required^{15,36}.

To remedy this problem, based on various interpretations and formulations of quantum theory, several attempts have been made to introduce a suitable arrival time distribution. On the one hand, according to the (generalized) standard canonical interpretation, the arrival distribution is considered as a generalized observable, which is described by a positive-operator-valued measure (POVM), satisfying some required symmetries^{11,12,37,38}.

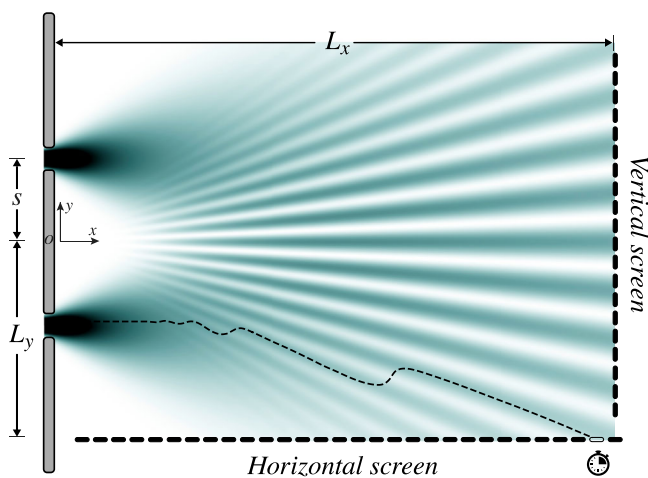


Fig. 1 Schematic double-slit experiment setup. The center of two slits is considered as the coordinate origin and the distance between the two slits is $2s$. The vertical and horizontal screens are placed at $x = L_x$ and $y = L_y$, respectively. The dashed black line shows a typical Bohmian trajectory—with recursive movements—that arrives at the horizontal screen. A suitable single-particle detector, in addition to particle arrival position, can record the arrival time using a proper clock.

On the other hand, in the realistic-trajectory-based formulations of quantum theory, such as the Bohmian mechanics³⁹, Nelson stochastic mechanics⁴⁰, and many interacting worlds interpretation⁴¹, the arrival time distribution could be obtained from particles trajectories^{7,20,21,42,43}. Moreover, in other approaches, the arrival time distribution is computed via phenomenological modeling of the detection process, such as the (generalized) path integral formalism in the presence of an absorbing boundary^{14,44–46}, Schrödinger equation with complex potential or absorbing boundary^{47–51}, and so on^{52–58}.

In principle, the results of these approaches are different. However, in most of the experimental situations, the differences are typically slight, and so far as we know, in the situation where differences are significant, none of the proposals have been backed up by experiments in a strict manner^{8,43}. An experiment that can probe these differences would undoubtedly enrich our understanding of the foundations of quantum mechanics. The purpose of the present paper is to make it evident, via numerical simulations, that the famous two-slit experiment could be utilized to investigate these differences if we simply use a horizontal screen instead of a vertical one: see Fig. 1. Using current laser cooling and magneto-optical trapping technologies, this type of experiment can be realized by Bose-Einstein condensates, as a controllable source of coherent matter waves^{59–61}. Moreover, our numerical study shows that the required space-time resolution in particle detection is achievable using fast single-atom detectors, such as the recent delay-line detectors described in ref. ^{62,63} or the detector used in ref. ^{6,64}.

Results and discussion

Spatiotemporal arrival distribution. Here we investigate the spatiotemporal arrival distribution of particles in an unconventional double-slit experiment with a horizontal screen instead of a vertical one, and contrast the predictions of different interpretations and formulations of quantum theory. As we have discussed in Supplementary Note 1, in the vertical screen case, there is no significant difference between the different methods' predictions. As shown in Fig. 1, the setup consists of two identical slits at $y = \pm s$, and screens are placed at $x = L_x$ and $y = L_y$, correspond to the vertical and horizontal screens, respectively. To avoid the mathematical complexity of Fresnel diffraction at the sharp-edge slits, it is supposed that the slits have soft edges that generate waves having identical Gaussian profiles in the y -direction. So we can take the wave function as an uncorrelated two-dimensional Gaussian wave packet, $\psi(x, y, t) = N[G_{u_x}^{\sigma_x}(y - s, t) + G_{u_y}^{\sigma_y}(y + s, t)]G_{u_x}^{\sigma_x}(x, t)$, where $G_u^{\sigma}(x, t) = (2\pi s_t^2)^{-1/4} \exp[(x - ut)^2/4\sigma_s + imu(x - \frac{ut}{2})/\hbar]$, with N the normalization constant, m the particle's mass, σ the initial dispersion, u the wave packet's velocity, and $s_t = \sigma(1 + iht/(2m\sigma^2))$. This form of Gaussian superposition state is commonly used in the literature^{7,65–68} and is feasible to implement by quantum technologies because such a state could be produced and controlled readily^{69,70}, even without using slits⁶⁰. Moreover, one can generalize this wave function by adding a relative phase between wave packets which is discussed in Supplementary Note 2. In our proposed setup, we have chosen the metastable helium atom, with mass $m = 6.64 \times 10^{-27}$ kg, as the interfering particle, and the parameters as $s = 10 \mu\text{m}$, $\sigma_x = 0.04 \mu\text{m}$, $\sigma_y = 0.5 \mu\text{m}$, $u_x = 3 \text{ms}^{-1}$, and $u_y = 0$. These values are feasible according to the performed experiments⁷¹. Moreover, the metastable helium atom could be detected with high efficiency because of its large internal energy^{63,72}.

In this experiment, the most general experimentally measurable distribution is joint spatiotemporal arrival distribution on the screen surface \mathbb{S} , denoted by $\mathbb{P}(\mathbf{x}, t|\mathbf{x} \in \mathbb{S})$, which is also called screen

observable¹². From this joint distribution, one can derive other arrival distributions, such as the marginal arrival time distribution at the screen, $\Pi(t|\mathbf{x} \in \mathbb{S})$, the conditional local arrival time distribution at a specific point \mathbf{x} on the screen, $\Pi_{\mathbf{x}}(t|\mathbf{x} \in \mathbb{S})$, and the marginal cumulative arrival position distribution, $P(\mathbf{x}|\mathbf{x} \in \mathbb{S})$. To calculate \mathbb{P} , we consider the main proposed approaches that are based on various interpretations and formulations of quantum theory, including the Semiclassical (SC) approximation, and the Standard (STD), Quantum Flux (QF), Bohmian Truncated Current (BTC), Absorbing Boundary Rule (ABR), and Path Integral with Absorbing Boundary (PAB) methods. These approaches are described and discussed in detail in the Methods section. In brief, these methods can be divided into two categories. In the first category, it is assumed that an ideal detector before particle detection does not affect the evolution of the wave function. This category includes the SC, STD, QF, and BTC methods, and is referred to as intrinsic or ideal methods. In the second category, which includes ABR and PAB methods, the detector back-effect is considered. In the SC method, it is assumed that particles move classically between the preparation and measurement. Therefore, the arrival time randomness is understood as a result of the uncertainty of momentum, and the arrival time distribution is obtained from momentum distribution as

$$\mathbb{P}_{\text{SC}}(\mathbf{x}, t|\mathbf{x} \in \mathbb{S}) = N_{\text{SC}} m^3 t^{-4} |\psi(\mathbf{x}, t)|^2 \int_{\mathbb{S}} |\tilde{\psi}_0(m\mathbf{x}/t)|^2 \mathbf{x} \cdot d\mathbf{S}, \quad (1)$$

where $\tilde{\psi}_0$ is the initial wave function in momentum representation, and N_{SC} is the normalization constant. The STD method is based on defining a proper arrival time operator, and the joint arrival distribution is obtained as

$$\mathbb{P}_{\text{STD}}(\mathbf{x}, t|\mathbf{x} \in \mathbb{S}) = \sum_{\alpha=\pm} |\psi_{\mathbb{S}}^{\alpha}(\mathbf{x}, t)|^2. \quad (2)$$

where $\psi_{\mathbb{S}}^{\pm}(\mathbf{x}, t)$ is Kijowski's wave function, which is defined using eigenstates of the arrival time operator. On the other hand, inspired by Bohmian and some other formulations, many physicists would agree that the joint arrival distribution is given by the absolute value of the perpendicular component of the quantum probability current to the screen surface as

$$\mathbb{P}_{\text{QF}}(\mathbf{x}, t|\mathbf{x} \in \mathbb{S}) = N_{\text{QF}} |\mathbf{J}(\mathbf{x}, t) \cdot \mathbf{n}|, \quad (3)$$

where $\mathbf{J}(\mathbf{x}, t) = -\hbar m^{-1} \text{Im}[\psi_t^*(\mathbf{x}) \nabla \psi_t(\mathbf{x})]$, N_{QF} is the normalization constant, and \mathbf{n} is the outward normal to the screen \mathbb{S} . In the BTC method, as another version of QF, instead of the usual quantum current, the Bohmian truncated current, $\tilde{\mathbf{J}}(\mathbf{x}, t)$, is used to ensure that Bohmian particles enter the detector only once, and we have

$$\mathbb{P}_{\text{BTC}}(\mathbf{x}, t|\mathbf{x} \in \mathbb{S}) = N_{\text{BTC}} |\tilde{\mathbf{J}}(\mathbf{x}, t) \cdot \mathbf{n}|, \quad (4)$$

where N_{BTC} is the normalization constant. Note that, the Bohmian truncated current is defined using Bohmian trajectories and is computed numerically. Another proposed way to consider the detector effect is by using a proper boundary condition on the screen. In this regard, in the ABR method, we have

$$\mathbb{P}_{\text{ABR}}(\mathbf{x}, t|\mathbf{x} \in \mathbb{S}) = N_{\text{ABR}} |\psi_{\text{ABC}}(\mathbf{x}, t)|^2, \quad (5)$$

where N_{ABR} is the normalization constant, and ψ_{ABC} represent the solution of the free Schrödinger equation satisfying a Robin boundary condition, $\mathbf{n} \cdot \nabla \psi_{\text{ABC}} = i\kappa \psi_{\text{ABC}}$, where κ is a detector characterizing constant. Finally, using a generalized version of path integral formalism in the presence of an absorbing boundary, the joint arrival distribution is obtained as

$$\mathbb{P}_{\text{PAB}}(\mathbf{x}, t|\mathbf{x} \in \mathbb{S}) = N_{\text{PAB}} \frac{\lambda \hbar}{m\pi} |\mathbf{n} \cdot \nabla \psi_{\text{PAB}}(\mathbf{x}, t)|^2 \exp \left\{ -\frac{\lambda \hbar}{m\pi} \int_0^t dt' \oint_{\mathbb{S}} d\mathbf{S}' |\mathbf{n}' \cdot \nabla \psi_{\text{PAB}}(\mathbf{x}', t')|^2 \right\}, \quad (6)$$

where N_{PAB} is the normalization constant, and ψ_{PAB} is the solution of the Schrödinger equation satisfying the Dirichlet boundary condition, and λ is a proportionality factor with the dimension of length. The origins of these equations and the details of their derivation are brought up in the Methods section.

In Fig. 2, all the mentioned spatiotemporal distributions, \mathbb{P}_{SC} , \mathbb{P}_{STD} , \mathbb{P}_{QF} , \mathbb{P}_{BTC} , \mathbb{P}_{ABR} , and \mathbb{P}_{PAB} , are plotted for a horizontal screen located at $L_y = 15 \mu\text{m}$. These density plots clearly visualize the differences between the proposals. In this figure, one can see separated fringes with different shapes, which implies that the particles arrive at the screen in some detached space-time regions. In the insets, one can see that the shapes of these regions are different for each proposal. In the joint density of the semiclassical approximation (Fig. 2a), fringes are well-separated, while the standard distribution (Fig. 2b) exhibits more continuity in its fringes. In addition, in the pattern of the quantum flux proposal (Fig. 2c) there are grooves between every two fringes which are due to the changing of the sign of $\mathbf{J}(\mathbf{x}, t) \cdot \mathbf{n}$ in (3). In all panels of Fig. 2, the duration of *temporal no-arrival windows* between every two typical fringes varies in the range between 0.01 and 0.2 ms, which has a spatial extension of about 0.3–2 mm. These space-time scales are utterly amenable empirically by current technologies^{64,71}, which could be used to test these results. As one can see, the distributions of the ABR and PAB methods—i.e., Fig. 2d, e—have more compatibility with each other than the result of the BTC method. However, there are differences between them which are more obvious in the zoomed areas. The joint density of the ABR is more uniformly distributed than that of the PAB method. The empty areas between the fringes in Fig. 2f are due to the elimination of second and third arrivals in the recursive trajectories, which we discuss in the Detection schemes subsection. In the following subsections, we analyze the predictions of the different approaches and models about the marginal arrival distributions and discuss more about the feasibility of our proposed experiment.

Detailed comparison between intrinsic arrival distributions. To calculate the intrinsic marginal arrival distribution of each method, one could simply integrate the joint arrival distribution over the screen surface \mathbb{S} as $\Pi(t|\mathbf{x} \in \mathbb{S}) = \int_{\mathbb{S}} \mathbb{P}(\mathbf{x}, t|\mathbf{x} \in \mathbb{S}) d\mathbf{S}$, with $d\mathbf{S} = \mathbf{n} \cdot d\mathbf{S}$ the magnitude of the surface element $d\mathbf{S}$ which is directed outward at $\mathbf{x} \in \mathbb{S}$. In this regard, in Fig. 3, the arrival time distributions at the screen are plotted for the horizontal screens located at $L_y = 30 \mu\text{m}$ in panel (a), $L_y = 25 \mu\text{m}$ in panel (b), $L_y = 20 \mu\text{m}$ in panel (c), and $L_y = 15 \mu\text{m}$ in panel (d). In this figure, solid-black, dashed-green, and dash-dotted-blue curves represent the distributions Π_{STD} , Π_{QF} and Π_{SC} , respectively. Also, the vertical lines show the average time of arrival to the screen, $\bar{t}_{\mathbb{S}}$, associated with these arrival time distributions, which could be calculated as

$$\bar{t}_{\mathbb{S}} = \int_0^{\infty} dt \Pi(t|\mathbf{x} \in \mathbb{S}) t. \quad (7)$$

As one can see in Fig. 3, as the screen's distance from the center of the two slits L_y decreases, the difference between distributions and average arrival times increases. Most of these differences occur in the early times, which are associated with the particles that arrive at the \mathbb{S} in the near field. Furthermore, we observe that the Π_{SC} behaves quite differently from Π_{QF} and Π_{STD} . The distributions Π_{QF} and Π_{STD} are more or less in agreement for larger L_y , however, for the screen that is located at $L_y = 15 \mu\text{m}$, a significant difference between the standard and quantum flux distributions occurs around $t \approx 0.2$ ms.

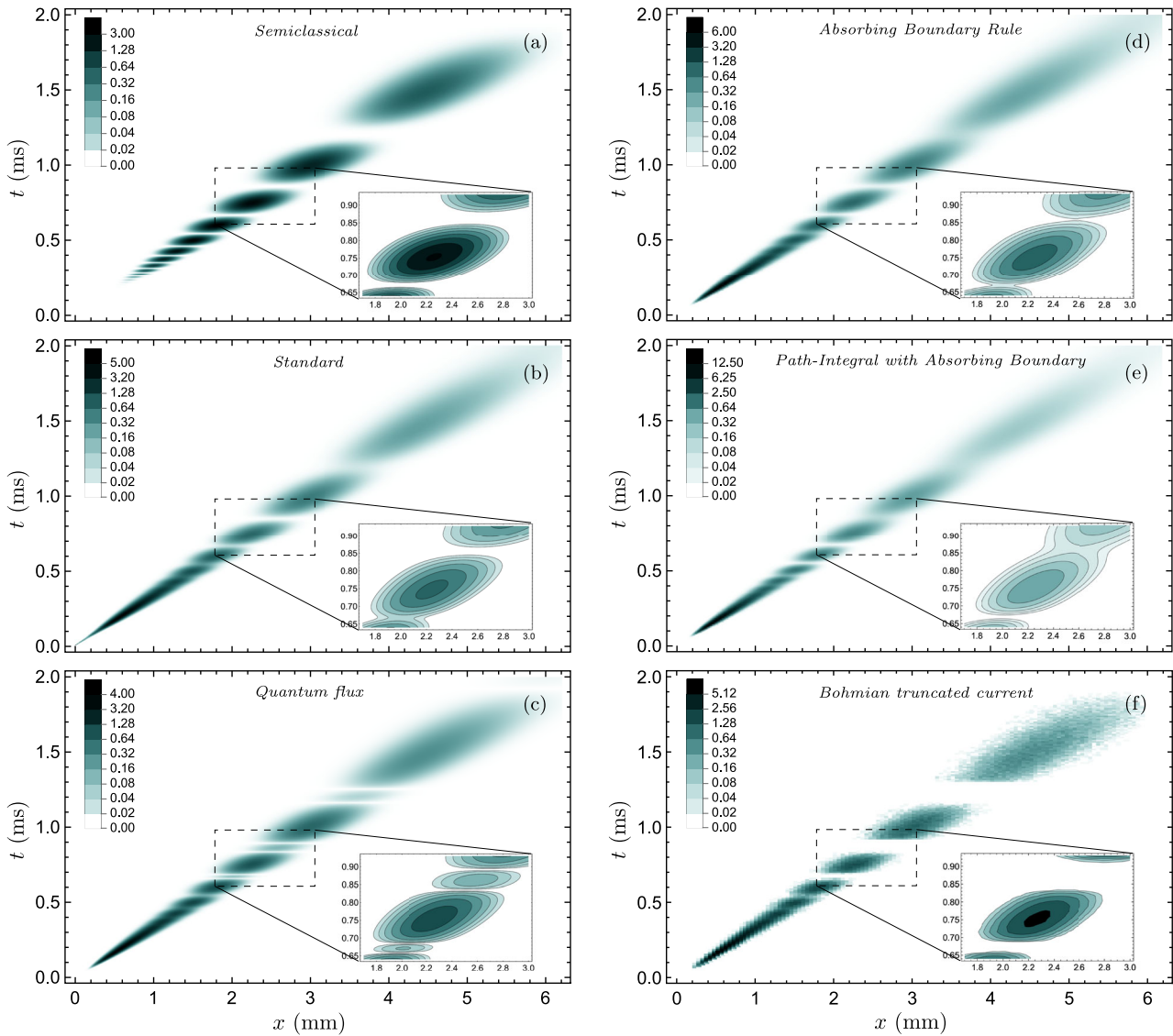


Fig. 2 Joint spatiotemporal probability distributions on the horizontal screen of the double-slit setup. **a–c** Represent intrinsic distributions predicted by the semiclassical approximation, standard method, and quantum flux approach, respectively. Panel **d, e** are the joint arrival distributions predicted by methods that take the screen back-effect into account, i.e., absorbing boundary role and path integral with absorbing boundary, respectively. Panel **(f)** is the joint arrival distribution obtained by Bohmian truncated current that is calculated numerically by simulating 10^7 Bohmian trajectories. Insets: Magnified contour plots of the joint distributions.

Furthermore, we can compute the average arrival time to each point on the screen using the joint probability distribution as

$$\bar{t}_{\mathbf{x}} = \frac{\int_0^\infty dt \mathbb{P}(\mathbf{x}, t | \mathbf{x} \in \mathbb{S}) t}{\int_0^\infty dt \mathbb{P}(\mathbf{x}, t | \mathbf{x} \in \mathbb{S})}, \quad (8)$$

and the cumulative position interference pattern can be calculated as

$$P(\mathbf{x} | \mathbf{x} \in \mathbb{S}) = \frac{\int_0^\infty dt \mathbb{P}(\mathbf{x}, t | \mathbf{x} \in \mathbb{S})}{\int_0^\infty dt \int_{\mathbb{S}} d\mathbb{S} \mathbb{P}(\mathbf{x}, t | \mathbf{x} \in \mathbb{S})}. \quad (9)$$

In panels (a) and (b) of Fig. 4, these two quantities are shown for the horizontal screen which is placed at $y = 15 \mu\text{m}$. In contrast to the vertical screen, the cumulative position distribution of the semiclassical approximation is entirely separate from the two other proposals. The cumulative position distribution resulting from standard and quantum flux approaches have obvious differences from each other, as well. As one can see in panel (b) of Fig. 4, the average arrival times are the same for all three methods

at first and begin to deviate from each other around $x \approx 5 \text{ mm}$, then again, these curves converge to each other around $x \approx 25 \text{ mm}$, approximately. The maximum deviation between the standard and quantum flux average arrival time occurs at $x \approx 19 \text{ mm}$, which is quite in the far-field regime—the width of the initial wave function is $\sim O(10^{-3}) \text{ mm}$ which is $\ll 19 \text{ mm}$. Therefore, one can suggest the average arrival time in the gray region of the panel (b) of Fig. 4 as a practical target for comparing these approaches experimentally. To this end, we study arrival time distributions at some points of this region as *local arrival distributions*. The arrival time distribution conditioned at a specific point \mathbf{x} on the screen can be obtained as follows

$$\Pi_{\mathbf{x}}(t | \mathbf{x} \in \mathbb{S}) = \frac{\mathbb{P}(\mathbf{x}, t | \mathbf{x} \in \mathbb{S})}{\int_0^\infty dt \mathbb{P}(\mathbf{x}, t | \mathbf{x} \in \mathbb{S})}. \quad (10)$$

Using the associated joint distribution of each proposal, we have plotted panels (c–f) of Fig. 4 that show $\Pi_{\mathbf{x}}(t | \mathbf{x} \in \mathbb{S})$ at the positions $x = 16.2, 17.4, 18.4, 19.2 \text{ mm}$, on the screen placed at

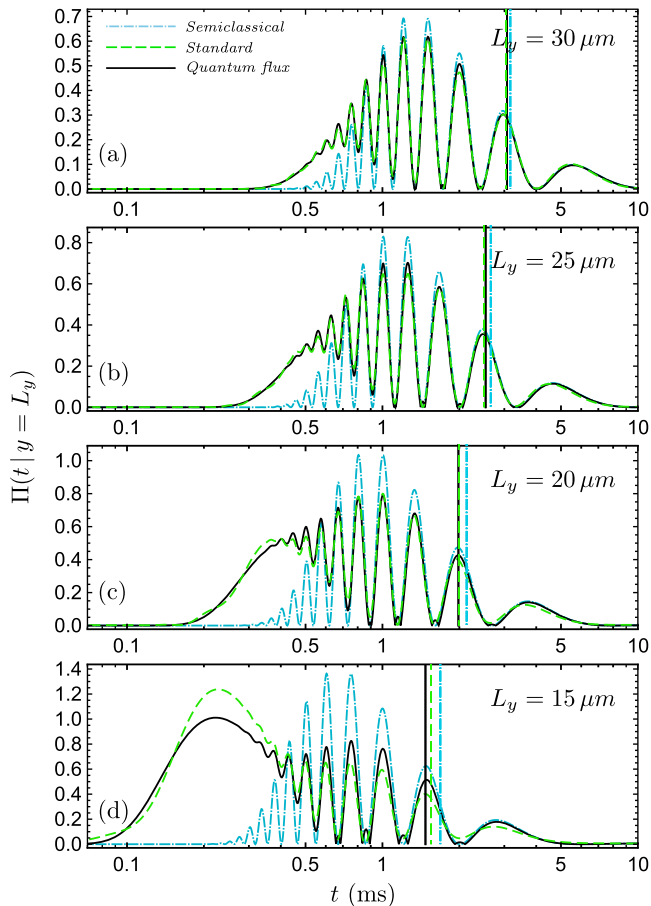


Fig. 3 Arrival time distributions at the horizontal screen of the double-slit setup. **a–d** Show the arrival distribution, $\Pi(t|y=L_y)$, at different screen distances $L_y = 30, 25, 20, 5 \mu\text{m}$, respectively. The vertical lines show the average arrival time. In all panels, the dark cyan dot-dashed lines show the semiclassical approximation, the green dashed lines show the standard method, and the black solid lines show the quantum flux approach.

$L_y = 15 \mu\text{m}$. The broken black curves in these panels, resulting from the quantum flux proposal, contrast with the smooth curves of the other two methods, which could be understood as the result of the changing of the signature of the y -component of the probability current: Note that, quantum flux distribution is given by the absolute value of the probability current. The origin of distinctions between the local average arrival times is more perceptible from these local arrival distributions. In principle, these distributions could be probed using fast and high-resolution single-atom detectors^{64,72}. In particular, the delay-line detector that is recently developed by Keller et al.⁶² seems suitable for our purpose: it has the capability to resolve single-atom detection events temporally with 220 ps and spatially with 177 μm at rates of several 10^6 events per second.

We estimate by a numerical investigation that these local arrival distributions could be well reconstructed from about 10^4 number of detection events. As an example, in Fig. 4, the histograms associated with the probability densities in panel (f) are plotted in panel (g), using 10^4 numerical random sampling. It is easy to estimate that the recording of 10^4 particle detection events can determine the local average arrival time with a statistical error of about 10^{-2} ms, while the differences between local average arrival times of various proposals are almost $>10^{-1}$ ms. Using cumulative position distribution, Fig. 4b, one can estimate that, if the total number of particles that arrived at the screen is about 10^8 , we have about 10^4 particles around

$x = 19.2 \text{ mm}$, in the spacial interval (19.1, 19.3). Using recent progress in laser cooling and magneto-optical trapping⁷², the preparation of a coherent ensemble of metastable helium atoms with this number of particles is quite achievable⁶².

One might be inclined to think that the difference between the quantum flux and standard average arrival times is just due to changing the signature of $\mathbf{J}(\mathbf{x}, t) \cdot \mathbf{n}$, but in the following, we show that even without the contribution of the negative part of $\mathbf{J}(\mathbf{x}, t) \cdot \mathbf{n}$, these proposals are significantly distinguishable.

Detection schemes. According to the Bohmian deterministic point of view, there are several possible schemes to detect arrived particles, especially for the horizontal screen surface on which we have recursive motions (see Figs. 1 and 5). One can assume that the horizontal screen is swept with a point-like detector that surveys all arrived particles at the screen surface \mathbb{S} , which we call spot-detection scheme. In this scheme, one option is to use a unilateral detector to detect arrived particles at the top or bottom of \mathbb{S} . In this case, the positive and negative parts of the quantum probability current correspond respectively to particles that arrive at the top or bottom of \mathbb{S} (as shown in Fig. 5a), and we must use Eq. (26) to calculate the screen observables. Additionally, we can choose a bilateral detector (or two unilateral detectors) that probes all particles that arrive from both sides of \mathbb{S} , along the time with several repeats of the experiment (as shown in Fig. 5b). In these circumstances (i.e. spot-detection scheme), there is no barrier—such as the one in Fig. 5c—in front of the particles before they reach the point of detection and we can use the quantum flux method to obtain the screen observables as in the previous subsection.

As we have shown in the methods section, whether the particles arrive from the top or bottom of \mathbb{S} , the absolute value of the quantum probability current yields the trajectories' density and consequently gives the joint distribution of the total arrival at each point of \mathbb{S} . This fact is the case for the standard method, as well, however, there is a subtle difference between the two proposals in the spot-detection scheme. When we talk about the spot-detection in the Bohmian approach, it would be considered the possibility of multi-crossing and the distribution includes all-arrivals at \mathbb{S} . Although, in the standard method there is an interpretation for $\psi_{\mathbb{S}}^+(\mathbf{x}, t)$ and $\psi_{\mathbb{S}}^-(\mathbf{x}, t)$ in Eq. (21), which relates them to the particles that arrive at \mathbb{S} in a direction which is the same or opposite with the direction of outward normal of the screen \mathbf{n} , respectively^{11,73}. Nevertheless, it should be noted that, in contrast to the Bohmian interpretation, since there is no defined particle trajectory in the standard interpretation, it is meaningless to ask whether it only counts the *first arrivals* to each side of the screen or includes recursive movements of particles. In standard quantum mechanics, there is only one arrival because once a measurement has been made the state of the particle is not causally connected to the initial state⁷⁴.

Alternatively, along with the spot-detection scheme, it could be assumed that there is a continuous flat barrier in front of the particle's paths as the detection surface or screen surface that does not allow particles to cross this surface. Depending on the screen's length and position, there are several possibilities for the detection process. In each case, a specific number of particle paths contribute to the distribution of arrival time. In the simplest case, the screen blocks all the trajectories that reach the horizontal surface \mathbb{S} , and we only detect the first-arrivals. In such a setup, we can no longer use the quantum flux method to represent Bohmian trajectories' first encounter with the surface; hence, the screen observables must be obtained by numerical analysis, due to the definition of truncated current as in Eq. (27) and its corresponding joint distribution, $\mathbb{P}_{\text{BTC}}(\mathbf{x}, t|\mathbf{x} \in \mathbb{S})$, defined in

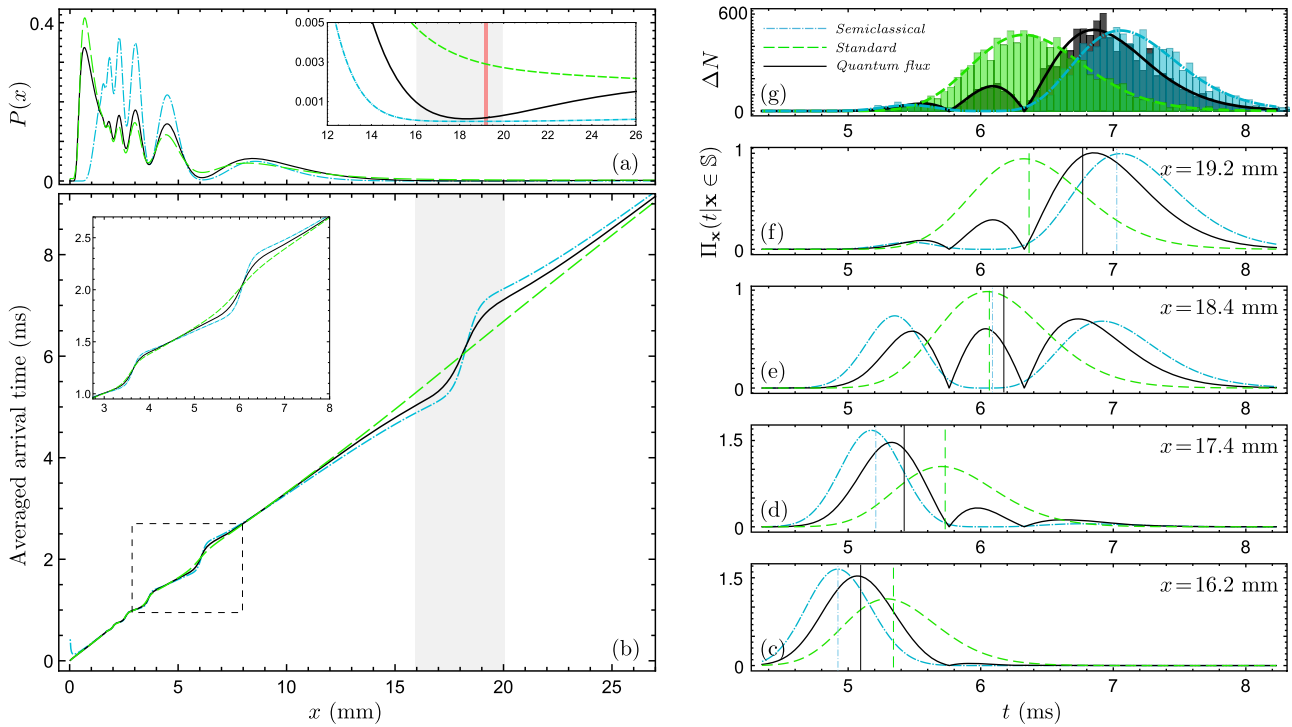


Fig. 4 Spatiotemporal arrival statistics for the double-slit experiment with a horizontal screen. **a** Represents the cumulative arrival position probability density. The inset of this panel is a zoom-in of the main plot close to the horizontal axis. **b** Shows the average time of arrival at each point of the screen. The inset of this panel is a zoom-in of the area marked with the dashed square in the main plot. **c–f** show the local arrival time probability densities, $\Pi_{\mathbf{x}}(t|\mathbf{x} \in \mathbb{S})$, at the points $x = 16.2, 17.4, 18.4, 19.2$ mm on the screen \mathbb{S} placed at $y = 15 \mu\text{m}$, respectively, which are chosen from the gray region in panel **(b)**. The vertical lines in these panels represent the average arrival times. **g** Contains the Histograms associated with the probability densities of the **(f)**, which are generated by 10^4 numerical random sampling. In all panels, the dark cyan dot-dashed lines show the semiclassical approximation, the green dashed lines show the standard method, and the black solid lines show the quantum flux approach.

Eq. (28). By computing the Bohmian trajectories, we can find positions and times of the first-arrivals to the screen, and consequently calculate the arrival time distribution which mathematically could be defined as

$$\Pi_{\text{BTC}}(t|\mathbf{x} \in \mathbb{S}) = \int_{\mathbb{S}} \mathbb{P}_{\text{BTC}}(\mathbf{x}, t|\mathbf{x} \in \mathbb{S}) d\mathbb{S}. \quad (11)$$

Also, other observable quantities such as the cumulative spatial distribution and averaged arrival time over the detection surface could be defined and calculated numerically in a similar way—by substituting $\mathbb{P}_{\text{BTC}}(\mathbf{x}, t|\mathbf{x} \in \mathbb{S})$ in Eqs. (8) and (9). Furthermore, we can complete the computations to find the second and third encounters to the surface (regardless of the barrier).

In Fig. 6, we show our numerical results of Bohmian trajectories simulation. The background scatter plot is the position and time of arrivals of 2×10^6 trajectories. In this plot, the second and third arrivals are shown in blue and green, respectively. Here, it is more clear why we interpret the grooves of the quantum flux density plot (Fig. 2c) as a result of the multi-crossing of Bohmian trajectories. The three middle graphs are the average time of the first and all-arrivals, which are simulation results of 10^8 trajectories, and are compared by the quantum flux method. As expected, the average time of all-arrivals fits on the quantum flux curve. However, the average time of first-arrivals deviates from all-arrivals in the area discussed in the previous section (between $x = 16.2$ mm and $x = 19.2$ mm).

To scrutinize the deviation zone of Fig. 6 (the gray region), Fig. 7 is drawn to show the arrival time distributions at the screen positions $x = 19.2$ mm in panel (a), $x = 18.4$ mm in panel (b), $x = 17.4$ mm in panel (c), and $x = 16.2$ mm in panel (d). As one can see, at the first recursive points of quantum flux distribution,

the first-arrival distributions drop down to zero. This implies that in the presence of a barrier-like screen, there would be a big temporal gap in the local arrival distribution at these points. These gaps could be investigated as a result of the non-intersection property of Bohmian trajectories that causes a unilateral motion of particles along the direction of the probability current field.

Screen back-effect. In order to complete the investigations carried out in previous subsections, we are going to study the screen back-effect in the double-slit experiment with a horizontal screen. In this regard, we compare the arrival distributions that result from the absorbing boundary rule (ABR), path-Integral with absorbing boundary (PAB), and Bohmian truncated current (BTC).

We continue with the same initial conditions as in previous subsections. Also, for each method there is a constant characterizing the type of detector which we explain in method section. We choose the characterizing constant of ABR method as $\kappa = 1 \mu\text{m}^{-1}$. This value of κ leads to the maximum absorption probability—which is almost 0.4—for the chosen initial wave function. In addition, for a more meaningful comparison, we consider the proportionality factor of PAB method as $\lambda = 1 \mu\text{m}$, which leads to the same absorption probability as ABR. In Fig. 8, the spatial and temporal marginal distributions are shown in panels (a) and (b), respectively. In addition, in panel (c), the associated local average arrival times are compared. The PAB method leads to significant discrepancies in marginal distributions; the maximum difference is about 40% that occurs around $x \approx 0.8$ mm, which seems testable clearly. In contrast to the previous results on intrinsic distributions, in which the difference

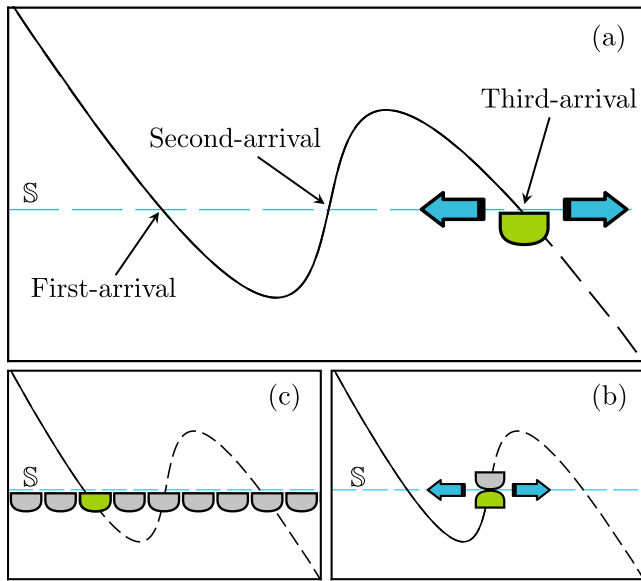


Fig. 5 Different schemes of particle detection on the screen surface S. In the Bohmian point of view, particles could have a recursive motion on surface \mathbb{S} and cross it more than once (e.g. see the plotted trajectory in Fig. 1). Assuming different detector types, one can probe variant possible observables on the screen. In **(a)** a conceivable particle trajectory is depicted, which crosses \mathbb{S} three times. In this panel, a movable point-like detector is placed on \mathbb{S} , which can survey the whole screen and detect particles that arrive only from one side, while in **(b)** a two-sided point detector is placed on \mathbb{S} , which can move along it and detect particles that arrive from up and down. In addition, one can assume there is **(c)** an array of side-by-side detectors covering the entire screen surface \mathbb{S} . The last configuration blocks the trajectory and does not allow the crossed particle to return. In this scheme, we only detect first-arrivals from one side.

between average arrival times was significant, there is a good agreement in this observable for the ABR and PAB methods. However, there is a significant difference between the average arrival time in these two methods and BTC around $x \approx 6$ mm. In Fig. 7, the local arrival time distributions at some points on the screen are plotted, which show similar behavior.

Conclusions

When and where does the wave function collapse? How one can model a detector in quantum theory? These are the questions that we investigated in this work. We tried to show that there is no agreed-upon answer for these questions, even for the double-slit experiment that has in it the heart of quantum mechanics⁷⁵. This is a practical encounter with the measurement problem⁷⁶. In this regard, we numerically investigated and compared the main proposed answers to these questions for a double-slit setup with a horizontal detection screen. It is shown that these proposals lead to experimentally distinguishable predictions, thanks to the current single-atom detection technology.

In this work, we suggest the metastable helium atom as a proper coherent source of the matter wave, however, other sources may lead to some practical improvements. For example, using heavier condensate atoms can lead to more clear discrepancies. Recently, S. Roncallo and coworkers suggest an interesting experiment, using the ⁸⁷Rb Bose-Einstein condensate trapped in an accelerator ring⁷⁷, to probe the various arrival time proposals⁵⁵. Moreover, pairs of entangled atoms, for example in a double-double slit setup, may lead to predictions that are more distinguishable^{20,21,78}.

Finally, it is worth noting that, although the experiment with photons may have some practical advantages, there are more complications in its theoretical analysis. This is partially because of the relativistic localization-causality problem^{24,79–81}. The theoretical investigation of the proposed experiment for photons would be an interesting extension of the present work, which has been left for future studies.

Methods

Intrinsic arrival distributions. In this subsection, we first review the semiclassical approximation and then scrutinize two main proposed intrinsic arrival time distributions^{18,43} and their associated screen observables. In these approaches, the effect of the detector’s presence on the wave function evolution, before particle detection, is not considered. We discuss this effect in the next subsection.

Semiclassical approximation. As mentioned, in the experiments in which the detectors are placed far away from the support of the initial wave function (i.e. far-field regime), the semiclassical arrival time distribution is routinely used to the description of the particle time-of-flight^{29,82–85}. In this approximation, it is assumed that particles move classically between the preparation and measurement. In this approach, the arrival time randomness is understood as a result of the uncertainty of momentum, and so the arrival time distribution is obtained from momentum distribution^{15,19,43,86}. In the one-dimensional case, the classical arrival time is given by

$$t = m(L - x_0)/p_0, \tag{12}$$

which is applicable for a freely moving particle of mass m that at the initial $t = 0$ had position x_0 and momentum p_0 arriving at a distant point L on a line. Hence, for a particle with the momentum wave function $\tilde{\psi}_0(p)$, assuming $\Delta x_0 \ll |L - \langle x \rangle_0|$, the semiclassical arrival time distribution reads⁸⁶

$$\Pi_{sc}(t|x = L) = \frac{mL}{t^2} |\tilde{\psi}_0(mL/t)|^2. \tag{13}$$

This analysis could be generalized in three-dimensional space. Then, the distribution of arrival time at a screen surface \mathbb{S} is given by⁴³

$$\Pi_{sc}(t|\mathbf{x} \in \mathbb{S}) = \frac{m^3}{t^4} \int_{\mathbb{S}} |\tilde{\psi}_0(m\mathbf{x}/t)|^2 \mathbf{x} \cdot d\mathbb{S}, \tag{14}$$

where the $d\mathbb{S}$ is the surface element directed outward. The other main distribution that should be demanded is the joint position-time probability distribution on the screen, which is also called “screen observable”¹². Using the conditional probability definition, the joint probability of finding the particle in $d\mathbb{S}$ and in a time interval $[t, t + dt]$ could be written as $\mathbb{P}(\mathbf{x}, t|\mathbf{x} \in \mathbb{S})d\mathbb{S}dt = [\Pi(t|\mathbf{x} \in \mathbb{S})dt] \times [\mathbb{P}(\mathbf{x}|\mathbf{x} \in \mathbb{S}, t)d\mathbb{S}]$. In this regard, one can use the fact that $\psi_t(\mathbf{x})$ is the state of the system, conditioned on the time being t in the Schrödinger picture. This implies that $|\psi_t(\mathbf{x})|^2$ refers to the position probability density conditioned at a specific time^{t6,17,87}. Therefore, in the semiclassical approximation, the joint spatiotemporal probability density reads as

$$\mathbb{P}_{sc}(\mathbf{x}, t|\mathbf{x} \in \mathbb{S}) = N_{sc} \Pi_{sc}(t|\mathbf{x} \in \mathbb{S}) |\psi_t(\mathbf{x})|^2 \tag{15}$$

in which $N_{sc} \equiv 1/\int_{\mathbb{S}} d\mathbb{S} |\psi_t(\mathbf{x})|^2$ is the normalization constant, and $d\mathbb{S} = \mathbf{n} \cdot d\mathbf{S}$, where \mathbf{n} is the outward unit normal vector at $\mathbf{x} \in \mathbb{S}$.

Standard approach. The first attempts to investigate the arrival time problem, based on the standard rules of quantum theory, were made at the beginning of the 1960s by Aharonov and Bohm⁸⁸, and also Paul⁹⁹. This approach starts with a symmetric quantization of classical arrival time expression (12), as follows⁹⁰:

$$\hat{t}_{AB} = mL\hat{p}^{-1} - \frac{m}{2} (\hat{p}^{-1}\hat{x} + \hat{x}\hat{p}^{-1}), \tag{16}$$

where \hat{x} and $\hat{p} = -i\partial/\partial x$ are the usual position and momentum operators, respectively, and \hat{t}_{AB} is called the Aharonov-Bohm time operator. This operator satisfies the canonical commutation relation with the free Hamiltonian operator, $[\hat{t}_{AB}, \hat{p}^2/2m] = i\hbar$, which has been used to establish the energy-time uncertainty relation^{73,91}. However, although \hat{t}_{AB} is Hermitian (or symmetric in mathematics literature), it is not a self-adjoint operator⁹²—a fact that is in agreement with Pauli’s theorem. The origin of this non-self-adjointness can be understood as a result of the singularity at $p = 0$ in the momentum representation, $\hat{t}_{AB} \rightarrow (i\hbar m/2)(p^{-2} - 2p^{-1}\partial_p)$ ⁹². Nevertheless, although the (generalized) eigenfunctions of \hat{t}_{AB} are not orthogonal, they constitute an over-complete set and provide a POVM, which are used to define the arrival-time distribution as follows^{91,92}:

$$\Pi_{STD}(t|x = L) = \frac{1}{2\pi\hbar} \sum_{\alpha=\pm} \left| \int_{-\infty}^{\infty} dp \theta(\alpha p) \sqrt{\frac{|p|}{m}} \tilde{\psi}_i(p) e^{iLp} \right|^2, \tag{17}$$

where $\theta(\cdot)$ is Heaviside’s step function and $\tilde{\psi}_i(p)$ is the wave function in the momentum representation which could be obtained from the initial wave function

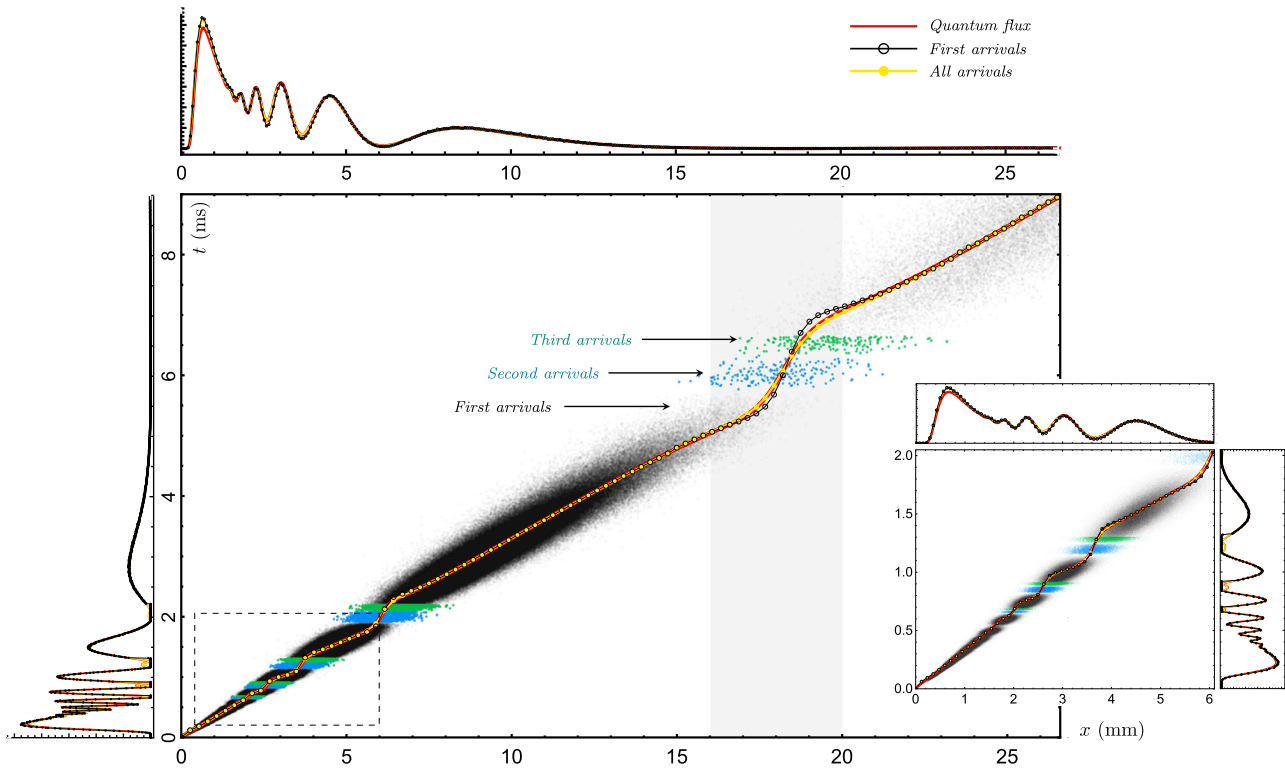


Fig. 6 Spatiotemporal Bohmian arrival statistics for the double-slit experiment with a horizontal screen. The interior curves in the central figure are the averaged times of arrival obtained by different detection schemes (see Fig. 5) using 10^8 simulated Bohmian trajectories. The left and top plots are marginal arrival time distributions and marginal arrival position distributions, respectively. The scatter plot is generated using 2×10^6 Bohmian trajectories, and the black, blue, and green points of the scatter plot represent the first, second, and third arrivals of Bohmian particles to the screen, respectively. The inset is a zoom-in of the dashed rectangle. The red solid lines represent the quantum flux approach, the black solid lines with empty circles markers show the first-arrivals scheme, and the yellow solid lines with filled circles show the all-arrivals scheme.

$\tilde{\psi}_0(p)$, as $\tilde{\psi}_i(p) = \tilde{\psi}_0(p) \exp[-itp^2/2m\hbar]$. The distribution Π_{STD} and its generalization in the presence of interaction potential have been referred to as the “standard arrival-time distribution” by some authors^{18,93–96}. In fact, Grot, Rovelli, and Tate treated the singularity of (16) by symmetric regularization and obtained eq. (17) via the standard Born rule⁷³. The generalizations of Eqs. (16) and (17) in the presence of interaction potential have been investigated in various works^{18,38,74,76,97–100}. Using these developments, it has been shown that the non-self-adjointness of the free arrival time operator can also be lifted by spatial confinement^{98,101}, and the above arrival time distribution could be derived from the limit of the arrival time distribution in a confining box as the length of the box increases to infinity⁹⁹. Furthermore, recently, the distribution (17) is derived from a space-time-symmetric extension of non-relativistic quantum mechanics¹⁰².

The three-dimensional generalization of (17) is derived by Kijowski’s¹¹ via an axiomatic approach. The assumed axioms are implied by the principle of the probability theory, the mathematical structure of standard quantum mechanics, and the Galilei invariance²⁶. Based on these axioms, Kijowski constructed the following arrival time distribution for a free particle that passes through a two-dimensional plane \mathbb{S} as

$$\Pi_{\text{STD}}(t|\mathbf{x} \in \mathbb{S}) = \frac{1}{2\pi\hbar} \sum_{\alpha=\pm} \int_{\mathbb{R}^2} d^2\mathbf{p}_{\parallel} \times \left| \int_{-\infty}^{\infty} dp_{\perp} \theta(\alpha\mathbf{p} \cdot \mathbf{n}) \sqrt{\frac{|\mathbf{p}_{\perp}|}{m}} \tilde{\psi}_i(\mathbf{p}) e^{i\mathbf{x} \cdot \mathbf{p}} \right|^2, \tag{18}$$

where $\mathbf{p}_{\perp} \equiv (\mathbf{p} \cdot \mathbf{n})\mathbf{n}$ and $\mathbf{p}_{\parallel} \equiv \mathbf{p} - \mathbf{p}_{\perp}$ are perpendicular and parallel components of \mathbf{p} relative to \mathbb{S} respectively, and \mathbf{n} is the outward normal of plane \mathbb{S} . In fact, he first proves the above expression for the wave functions whose supports lie in the positive (or negative) amounts of p_{\perp} . Then Kijowski *uniquely* derives the following self-adjoint variant of the (three-dimensional version of) Aharonov-Bohm arrival time operator, by demanding that the time operator be self-adjoint and leads to (18) for these special cases via the Born rule^{11,26}.

$$\hat{t}_L = \text{sgn}(\hat{p}_{\perp}) \left[mL\hat{p}_{\perp}^{-1} - \frac{m}{2} (\hat{p}_{\perp}^{-1}\hat{x}_{\perp} + \hat{x}_{\perp}\hat{p}_{\perp}^{-1}) \right], \tag{19}$$

where $\hat{x}_{\perp} \equiv \hat{\mathbf{x}} \cdot \mathbf{n}$ and $L (\equiv \mathbf{x} \cdot \mathbf{n})$ represent the distance between the detection surface and the origin. It is worth noting that, the presence of $\text{sgn}(\hat{p}_{\perp})$ operator ensures the self-adjointness of this time operator, however, leads to a modified commutation relation, i.e. $[\hat{t}_K, \hat{H}] = i\hbar \text{sgn}(\hat{p}_{\perp})$. Finally, for an arbitrary wave

function, the equation (18) could be derived from this self-adjoint operator. Moreover, considering this time operator, besides the components of the position operator in the detection plane, $\hat{x}_{\parallel} \equiv \hat{\mathbf{x}} - (\hat{\mathbf{x}} \cdot \mathbf{n})\mathbf{n}$, Kijowski obtains the following expression as the joint position-time distribution on the detection screen via the Born rule²⁶:

$$P_{\text{STD}}(\mathbf{x}, t|\mathbf{x} \in \mathbb{S}) = \sum_{\alpha=\pm} |\psi_{\mathbb{S}}^{\alpha}(\mathbf{x}, t)|^2, \tag{20}$$

in which $\psi_{\mathbb{S}}^{\pm}(\mathbf{x}, t)$ is the wave function on the basics of joint eigenstates of the operators \hat{t}_L and \hat{x}_{\parallel} . Explicitly

$$\psi_{\mathbb{S}}^{\pm}(\mathbf{x}, t) = \frac{1}{(2\pi\hbar)^{3/2}} \int d^3\mathbf{p} \theta(\pm\mathbf{p} \cdot \mathbf{n}) \sqrt{\frac{|\mathbf{p}_{\perp}|}{m}} \tilde{\psi}_i(\mathbf{p}) e^{i\mathbf{x} \cdot \mathbf{p}}. \tag{21}$$

Note that, the arrival time distribution (18) could be reproduced by taking the integral of (20) over the whole of the screen plane. The joint space-time probability distribution (20), and its generalization for the particles with arbitrary spin, have been also derived by Werner in another axiomatic manner¹². Moreover, it is easy to see that the results (18) and (20) can be obtained from a regularized version of the (three-dimensional generalization of) Aharonov-Bohm time operator, which is the same as the procedure used by Grot, Rovelli and Tate in one-dimensional cases⁷³. However, some paradoxical behaviors have been raised about this distribution which we discuss in Supplementary Note 3.

Quantum flux and Bohmian approach. Inspiring by classical intuition, another proper candidate for screen observables is the perpendicular component of the quantum probability current to the screen surface, $\mathbf{J}(\mathbf{x}, t) \cdot \mathbf{n}$, where

$$\mathbf{J}(\mathbf{x}, t) = -\frac{\hbar}{m} \text{Im} [\psi_i^*(\mathbf{x}) \nabla \psi_i(\mathbf{x})], \tag{22}$$

and \mathbf{n} is the outward normal to the screen \mathbb{S} . This proposal is applicable for a particle in a generic external potential and a generic screen surface, not necessarily an infinite plane. There are several attempts to derive this proposal in various approaches, such as Bohmian mechanics for the scattering case in²⁷, decoherent histories approach in¹⁰³ as an approximation, or in ref. ¹⁰⁴ as an exact formula using the concept of extended probabilities, and so on^{56,57,105}. However, even if the wave function contains only momentum in the same direction as \mathbf{n} , the $\mathbf{J}(\mathbf{x}, t) \cdot \mathbf{n}$

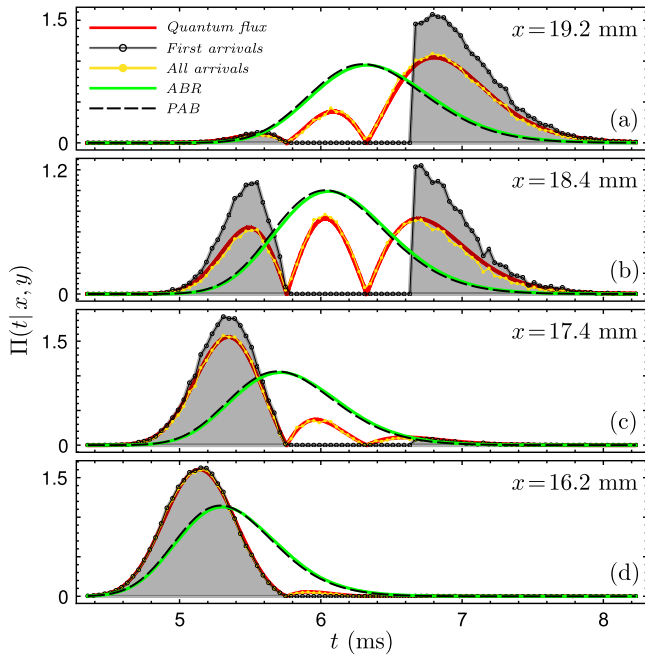


Fig. 7 Local arrival time distribution at some points of the horizontal screen in the double-slit setup. a–d Show the local arrival time probability densities, $\Pi_x(t|\mathbf{x} \in \mathbb{S})$, at the points $x = 16.2, 17.4, 18.4, 19.2$ mm on the screen \mathbb{S} placed at $y = 15 \mu\text{m}$, respectively, which are chosen from the gray region in Fig. 6. The black solid lines with empty circles markers show the first-arrivals scheme and the yellow solid lines with filled circles show the all-arrivals scheme. The width of numeric sampling of these two schemes in each point is about $\delta x = 0.25$ mm, and 10^8 Bohmian trajectories are simulated to obtain these distributions. The red solid lines represent the quantum flux approach, the green solid lines show the local arrival distributions obtained by absorbing boundary rule (ABR), and the black dashed lines show the local arrival distributions obtained by path-integral with absorbing boundary (PAB).

could be negative due to the *backflow* effect³⁰. This property is incompatible with the standard notion of probability.

Nevertheless, this problem could be treated from the Bohmian point of view: Using Bohmian trajectories, it can be shown that the positive and negative values of $\mathbf{J}(\mathbf{x}, t) \cdot \mathbf{n}$ correspond to the particles that reach the point \mathbf{x} at \mathbb{S} in the same direction of \mathbf{n} or the opposite direction of it, respectively^{106,107}. In this regard, through the Bohmian mechanics in one-dimension, Leavens demonstrates that the time distribution of arrival to $x = L$ from both sides could be obtained from the absolute form of probability flux as^{42,108}

$$\Pi_{\text{QF}}(t|x=L) = \frac{|\mathbf{J}(L, t)|}{\int dt |\mathbf{J}(L, t)|}, \quad (23)$$

which is free from the aforementioned problem. Furthermore, recently Juric and Nikolic have treated this problem from a different point of view⁵⁴. In the Juric-Nikolic analysis, the negative fluxes are interpreted as zero arrival probability density, which originates from a physical insight that in this case, the particle departs, rather than arrives.

The three-dimensional justification of $\mathbf{J}(\mathbf{x}, t) \cdot \mathbf{n}$ as an operational formulation of the arrival time model has been made in ref. ¹⁰⁵. Also, the generalization of (23) for arrival to the surface \mathbb{S} is given by^{7,15,18,109}

$$\Pi_{\text{QF}}(t|\mathbf{x} \in \mathbb{S}) = \frac{\int_{\mathbb{S}} dS |\mathbf{J}(\mathbf{x}, t) \cdot \mathbf{n}|}{\int dt \int_{\mathbb{S}} dS |\mathbf{J}(\mathbf{x}, t) \cdot \mathbf{n}|}, \quad (24)$$

with $dS = \mathbf{n} \cdot d\mathbf{S}$ the magnitude of the surface element $d\mathbf{S}$ which is directed outward at $\mathbf{x} \in \mathbb{S}$. To illustrate (24) and to generalize it to the case of joint arrival distribution, we can use the Bohmian point of view. In this theory, each particle has a specific trajectory, depending on the initial position, and so the rate of passing particles through an area element dS centered at $\mathbf{x} \in \mathbb{S}$, in the time interval between t and $t + dt$, is proportional to $\rho_t(\mathbf{x})|\mathbf{v}(\mathbf{x}, t) \cdot d\mathbf{S}|dt$, where $\mathbf{v}(\mathbf{x}, t) = \mathbf{J}(\mathbf{x}, t)/|\psi_t(\mathbf{x})|^2$ is the Bohmian velocity of the particle. Hence, using quantum equilibrium condition^{110,111}, $\rho_t(\mathbf{x}) = |\psi_t(\mathbf{x})|^2$, and accomplishing normalization, the joint arrival

distribution could be represented by the absolute value of the current density as

$$P_{\text{QF}}(\mathbf{x}, t|\mathbf{x} \in \mathbb{S}) = \frac{|\mathbf{J}(\mathbf{x}, t) \cdot \mathbf{n}|}{\int dt \int_{\mathbb{S}} dS |\mathbf{J}(\mathbf{x}, t) \cdot \mathbf{n}|}. \quad (25)$$

Now, by integrating (25) over all $\mathbf{x} \in \mathbb{S}$, we arrive at the three-dimensional arrival time distribution (24) for the screen surface \mathbb{S} . It should be noted that Eq. (25) is not necessarily followed for an ensemble of classical particles because a positive or negative current at a space-time point, (\mathbf{x}, t) , can in general have contributions from all the particles arriving to \mathbf{x} at t from any direction. Nonetheless, since the Bohmian velocity field is single-valued, the particle trajectories cannot intersect each other at any point of space-time and so only a single trajectory contributes to the current density $\mathbf{J}(\mathbf{x}, t)$ at the particular space-time point (\mathbf{x}, t) . Moreover, this fact implies that when $\mathbf{v}(\mathbf{x}, t) \cdot \mathbf{n} > 0$ we can say that the trajectory and consequently the particle has passed through the screen from the inside and vice versa for $\mathbf{v}(\mathbf{x}, t) \cdot \mathbf{n} < 0$. Hence, one can define the joint probability distribution for the time of arrival to each side of \mathbb{S} as

$$P_{\text{QF}}^{\pm}(\mathbf{x}, t|\mathbf{x} \in \mathbb{S}) = \frac{\mathbf{J}^{\pm}(\mathbf{x}, t) \cdot \mathbf{n}}{\int dt \int_{\mathbb{S}} dS \mathbf{J}^{\pm}(\mathbf{x}, t) \cdot \mathbf{n}}, \quad (26)$$

where $\mathbf{J}^{\pm}(\mathbf{x}, t) = \pm\theta(\pm \mathbf{J} \cdot \mathbf{n})\mathbf{J}(\mathbf{x}, t)$. In addition, note that there may be some trajectories which cross \mathbb{S} more than once—and we have *multi-crossing* trajectories (see the typical Bohmian trajectory in Fig. 1). The course of the above inference to Eq. (25) was in such a manner that multi-crossing trajectories could contribute several times (see Fig. 5a). However, one could assume the detection surface as a barrier that does not allow the crossed particle to return inside (see Fig. 5c). In this case, it is suggested to use the truncated current defined as

$$\tilde{\mathbf{J}}(\mathbf{x}, t) := \begin{cases} \mathbf{J}(\mathbf{x}, t) & \text{if } (\mathbf{x}, t) \text{ is a first exit through } \mathbb{S} \\ 0 & \text{otherwise} \end{cases} \quad (27)$$

where (\mathbf{x}, t) is a first exit event through the boundary surface \mathbb{S} , if the trajectory passing through \mathbf{x} at time t leaves inside \mathbb{S} at this time, for the first time since $t = 0$ ^{15,27,112}. The limiting condition in (27), imposes that the joint probability distribution based on it should be computed numerically using trajectories:

$$P_{\text{BTC}}(\mathbf{x}, t|\mathbf{x} \in \mathbb{S}) = \frac{\tilde{\mathbf{J}}(\mathbf{x}, t) \cdot \mathbf{n}}{\int dt \int_{\mathbb{S}} dS \tilde{\mathbf{J}}(\mathbf{x}, t) \cdot \mathbf{n}}. \quad (28)$$

Of course, the detection screen is not always a barrier-like surface (see Fig. 5b), and one could assume that there is a point-like detector that lets the multi-crossing trajectories to contribute to the distribution and we can use (25) in such cases.

Non-intrinsic arrival distributions. In principle, the presence of the detector could modify the wave function evolution, before the particle detection, which is called detector back-effect. To have a more thorough investigation of detection statistics, we should consider this effect. However, due to the measurement problem and the quantum Zeno effect^{10,113,114}, a complete investigation of the detector effects is problematic at the fundamental level, and it is less obvious how to model an ideal detector—there are some recent interesting papers that deal with these problems, especially in connection with arrival time problem^{50,54}. Nonetheless, some phenomenological non-equivalent models are proposed, such as the generalized Feynman path integral approach in the presence of absorbing boundary^{14,44–46}, Schrödinger equation with a complex potential⁵¹, Schrödinger equation with absorbing (or complex Robin) boundary condition^{47–51}, and so on⁵⁴. The results of these approaches are not the same, and a detailed study of the differences is an interesting topic. In this section, we provide a brief review of the absorbing boundary rule (ABR) and path-Integral with absorbing boundary (PAB) models, then we compare them in the double-slit setup with the horizontal screen.

Absorbing boundary rule. Among the above-mentioned phenomenological models, the absorbing boundary condition approach has the most compatibility with Bohmian mechanics⁴⁹. The application of absorbing boundary condition (ABC) in arrival time problem was first proposed by Werner⁴⁷, and recently it is re-derived and generalized by Tumulka and others using various methods^{48–51}. Especially, it is recently shown that in a suitable (non-obvious) limit, the imaginary potential approach yields the distribution of detection time and position in agreement with the absorbing boundary rule⁵¹. According to this rule, the particle wave function ψ evolves according to the free Schrödinger equation, while the presence of a detection screen is modeled by imposing the following boundary conditions on the detection screen, $\mathbf{x} \in \mathbb{S}$,

$$\mathbf{n} \cdot \nabla \psi = i\kappa \psi, \quad (29)$$

where $\kappa > 0$ is a constant characterizing the type of detector, in which $\hbar\kappa/m$ represents the momentum that the detector is most sensitive to. This boundary condition ensures that waves with wave number κ are completely absorbed while waves with other wave numbers are partly absorbed and partly reflected^{48,115}. In the absorbing boundary rule, the joint spatiotemporal distribution of the detection event is given by quantum flux. Considering (29), this distribution

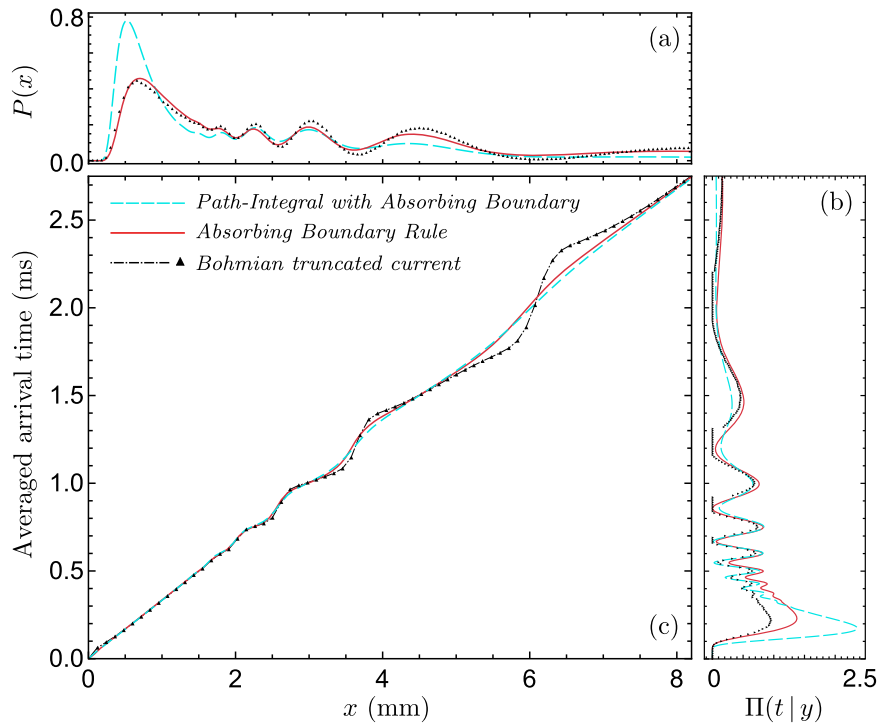


Fig. 8 Spatiotemporal arrival statistics for the double-slit experiment with absorbing horizontal screen. **a** Represents cumulative interference patterns, **(b)** shows arrival time distributions on the screen, and plots in **(c)** are the averaged time of arrival at each point of the screen. In all panels, the red solid lines represent the absorbing boundary rule, the cyan dashed lines correspond to the path-integral with absorbing boundary method, and black triangle markers belong to the plots obtained by Bohmian truncated current method.

reads

$$\mathbb{P}_{\text{ABR}}(\mathbf{x}, t | \mathbf{x} \in \mathbb{S}) = \frac{|\psi_{\text{ABC}}|^2}{\int dt \int_{\mathbb{S}} dS |\psi_{\text{ABC}}|^2}, \quad (30)$$

where ψ_{ABC} represent the solution of the free Schrödinger equation satisfying the aforementioned absorbing boundary condition. This distribution can be understood in terms of Bohmian trajectories. The Bohmian particle equation of motion, $\dot{\mathbf{X}} = (\hbar/m)\text{Im}[\nabla\psi_{\text{ABC}}/\psi_{\text{ABC}}]$, together with the boundary condition (29), imply that trajectories can cross the boundary \mathbb{S} only outwards and so there are no multi-crossing trajectories. If it is assumed that the detector clicks when and where the Bohmian particle reaches \mathbb{S} , the probability distribution of detection events is given by (30), because the initial distribution of the Bohmian particle is $|\psi_{\text{ABC}}(\mathbf{x}, 0)|^2$ ²⁴⁸.

Path-integral with absorbing boundary. In several papers^{14,44–46}, Marchewka and Schuss develop an interesting method to calculate the detection effect of absorbing surface using the Feynman path integral method. They postulate a *separation principle* for the wave function in which we could consider the (bounded wave function) as a sum of two parts, $\psi(\mathbf{x}, t) = \psi_1(\mathbf{x}, t) + \psi_2(\mathbf{x}, t)$, such that $\psi_1(\mathbf{x}, t)$ corresponds to the survival part of the wave which is orthogonal to $\psi_2(\mathbf{x}, t)$ at a time t and evolve independently⁴⁵. So, we can obtain the probability of survival of the particle, denoted $S(t)$, which is the probability of the particle not being absorbed by the time t , as $\int_{\mathbb{D}} d^3\mathbf{x} |\psi_1(\mathbf{x}, t)|^2$, where the integral is over the domain \mathbb{D} , outside the absorbing region. By discretizing the path integral in a time interval $[0, t]$ and eliminating the trajectories that, in each time interval $[t', t' + \Delta t']$ for all $t' < t$, are reached to the absorbing surface \mathbb{S} , the survival and consequently absorbing probability would be obtained. Based on this analysis, we could define a unidirectional probability current into the surface as $\frac{d}{dt}[1 - S(t)]$, which yields a normal component of the multidimensional probability current density at any point on \mathbb{S} as

$$\mathbf{J}(\mathbf{x}, t) \cdot \mathbf{n} = \frac{\lambda\hbar}{m\pi} |\mathbf{n} \cdot \nabla\psi(\mathbf{x}, t)|^2 \times \exp\left\{-\frac{\lambda\hbar}{m\pi} \int_0^t dt' \oint_{\mathbb{S}} dS |\mathbf{n} \cdot \nabla\psi(\mathbf{x}', t')|^2\right\}, \quad (31)$$

where $dS = \mathbf{n} \cdot d\mathbf{S}$ is the magnitude of the surface element $d\mathbf{S}$, \mathbf{n} is the unit outer normal to the absorbing surface \mathbb{S} , and λ is a proportionality factor with the dimension of length^{44,90}. Also, $\psi(\mathbf{x}, t)$ is the solution of Schrödinger equation bounded and normalized in the domain \mathbb{D} . Moreover, the normal component $\mathbf{J}(\mathbf{x}, t) \cdot \mathbf{n}$ is supposed to be the probability density for observing the particle at the point \mathbf{x} on the screen at time t ^{14,46}.

Data availability

The data that support the findings of this study are available from the corresponding author upon reasonable request.

Received: 20 January 2023; Accepted: 21 July 2023;

Published online: 31 July 2023

References

- Pauli, W. In *Encyclopedia of Physics* Vol. 5/1, 60 (Springer, Berlin, 1958).
- Zimmermann, Tcv, Mishra, S., Doran, B. R., Gordon, D. F. & Landsman, A. S. Tunneling time and weak measurement in strong field ionization. *Phys. Rev. Lett.* **116**, 233603 (2016).
- Kataoka, M. et al. Time-of-flight measurements of single-electron wave packets in quantum hall edge states. *Phys. Rev. Lett.* **116**, 126803 (2016).
- Kolenderski, P. et al. Time-resolved double-slit interference pattern measurement with entangled photons. *Sci. Rep.* **4**, 1–4 (2014).
- Frabboni, S. et al. The young-feynman two-slits experiment with single electrons: Build-up of the interference pattern and arrival-time distribution using a fast-readout pixel detector. *Ultramicroscopy* **116**, 73–76 (2012).
- Kurtsiefer, C., Pfau, T. & Mlynek, J. Measurement of the wigner function of an ensemble of helium atoms. *Nature* **386**, 150–153 (1997).
- Nitta, H. & Kudo, T. Time of arrival of electrons in the double-slit experiment. *Phys. Rev. A* **77**, 014102 (2008).
- Das, S., Nöth, M. & Dürr, D. Exotic bohmian arrival times of spin-1/2 particles: An analytical treatment. *Phys. Rev. A* **99**, 052124 (2019).
- Das, S., Deckert, D.-A., Kellers, L. & Struyve, W. Double-slit experiment remastered. *arXiv* <https://doi.org/10.48550/arXiv.2211.13362> (2022).
- Allcock, G. The time of arrival in quantum mechanics i. formal considerations. *Ann. Phys.* **53**, 253–285 (1969).
- Kijowski, J. On the time operator in quantum mechanics and the Heisenberg uncertainty relation for energy and time. *Rep. Math. Phys.* **6**, 361–386 (1974).
- Werner, R. Screen observables in relativistic and nonrelativistic quantum mechanics. *J. Math. Phys.* **27**, 793–803 (1986).
- Mielnik, B. The screen problem. *Found. Phys.* **24**, 1113–1129 (1994).

14. Marchewka, A. & Schuss, Z. Survival probability of a quantum particle in the presence of an absorbing surface. *Phys. Rev. A* **63**, 032108 (2001).
15. Vona, N., Hinrichs, G. & Dürr, D. What does one measure when one measures the arrival time of a quantum particle? *Phys. Rev. Lett.* **111**, 220404 (2013).
16. Maccone, L. & Sacha, K. Quantum measurements of time. *Phys. Rev. Lett.* **124**, 110402 (2020).
17. Dias, E. O. & Parisio, F. Space-time-symmetric extension of nonrelativistic quantum mechanics. *Phys. Rev. A* **95**, 032133 (2017).
18. Das, S. & Nöth, M. Times of arrival and gauge invariance. *Proc. R. Soc. A* **477**, 20210101 (2021).
19. Das, S. & Struyve, W. Questioning the adequacy of certain quantum arrival-time distributions. *Phys. Rev. A* **104**, 042214 (2021).
20. Kazemi, M. J. & Hosseinzadeh, V. Detection statistics in a double-double-slit experiment. *Phys. Rev. A* **107**, 012223 (2023).
21. Ayatollah Rafsanjani, A., Kazemi, M., Hosseinzadeh, V. & Golshani, M. Non-local interference in arrival time. <https://arxiv.org/abs/2307.04811> (2023).
22. Dürr, D., Goldstein, S. & Zanghi, N. Quantum equilibrium and the role of operators as observables in quantum theory. *J. Stat. Phys.* **116**, 959–1055 (2004).
23. Dürr, D. & Teufel, S. in *Multiscale Methods in Quantum Mechanics*, 41–58 (Springer, 2004).
24. Terno, D. R. Localization of relativistic particles and uncertainty relations. *Phys. Rev. A* **89**, 042111 (2014).
25. Sombillo, D. L. B. & Galapon, E. A. Particle detection and non-detection in a quantum time of arrival measurement. *Ann. Phys.* **364**, 261–273 (2016).
26. Kijowski, J. Comment on “arrival time in quantum mechanics” and “time of arrival in quantum mechanics”. *Phys. Rev. A* **59**, 897–899 (1999).
27. Daumer, M., Dürr, D., Goldstein, S. & Zanghi, N. On the quantum probability flux through surfaces. *J. Stat. Phys.* **88**, 967–977 (1997).
28. Shucker, D. S. Stochastic mechanics of systems with zero potential. *J. Funct. Anal.* **38**, 146–155 (1980).
29. Wolf, S. & Helm, H. Ion-recoil momentum spectroscopy in a laser-cooled atomic sample. *Phys. Rev. A* **62**, 043408 (2000).
30. Bracken, A. J. & Melloy, G. F. Probability backflow and a new dimensionless quantum number. *J. Phys. A: Math. Gen.* **27**, 2197 (1994).
31. Hofmann, H. F. Quantum interference of position and momentum: a particle propagation paradox. *Phys. Rev. A* **96**, 020101 (2017).
32. Korzh, B. et al. Demonstration of sub-3 ps temporal resolution with a superconducting nanowire single-photon detector. *Nat. Photonics* **14**, 250–255 (2020).
33. Steinhauer, S., Gyger, S. & Zwiller, V. Progress on large-scale superconducting nanowire single-photon detectors. *Appl. Phys. Lett.* **118**, 100501 (2021).
34. Azzouz, H., Dorenbos, S. N., De Vries, D., Ureña, E. B. & Zwiller, V. Efficient single particle detection with a superconducting nanowire. *AIP Adv.* **2**, 032124 (2012).
35. Rosticher, M. et al. A high efficiency superconducting nanowire single electron detector. *Appl. Phys. Lett.* **97**, 183106 (2010).
36. Delgado, F., Muga, J. G. & García-Calderón, G. Suppression of zeno effect for distant detectors. *Phys. Rev. A* **74**, 062102 (2006).
37. Hegerfeldt, G. C. & Muga, J. G. Symmetries and time operators. *J. Phys. A: Math Theor.* **43**, 505303 (2010).
38. Hegerfeldt, G. C., Muga, J. G. & Muñoz, J. Manufacturing time operators: covariance, selection criteria, and examples. *Phys. Rev. A* **82**, 012113 (2010).
39. Bohm, D. A suggested interpretation of the quantum theory in terms of “hidden” variables. i. *Phys. Rev.* **85**, 166–179 (1952).
40. Nelson, E. Derivation of the schrödinger equation from newtonian mechanics. *Phys. Rev.* **150**, 1079–1085 (1966).
41. Hall, M. J. W., Deckert, D.-A. & Wiseman, H. M. Quantum phenomena modeled by interactions between many classical worlds. *Phys. Rev. X* **4**, 041013 (2014).
42. Leavens, C. R. Time of arrival in quantum and Bohmian mechanics. *Phys. Rev. A* **58**, 840–847 (1998).
43. Das, S. & Dürr, D. Arrival time distributions of spin-1/2 particles. *Sci. Rep.* **9**, 2242 (2019).
44. Marchewka, A. & Schuss, Z. Feynman integrals with absorbing boundaries. *Phys. Lett. A* **240**, 177–184 (1998).
45. Marchewka, A. & Schuss, Z. Path-integral approach to the schrödinger current. *Phys. Rev. A* **61**, 052107 (2000).
46. Marchewka, A. & Schuss, Z. Measurement as absorption of feynman trajectories: Collapse of the wave function can be avoided. *Phys. Rev. A* **65**, 042112 (2002).
47. Werner, R. Arrival time observables in quantum mechanics. *Ann. l’IHP Phys. Théor.* **47**, 429–449 (1987).
48. Tumulka, R. Distribution of the time at which an ideal detector clicks. *Ann. Phys.* **442**, 168910 (2022).
49. Tumulka, R. Detection-time distribution for several quantum particles. *Phys. Rev. A* **106**, 042220 (2022).
50. Dubey, V., Bernardin, C. & Dhar, A. Quantum dynamics under continuous projective measurements: Non-hermitian description and the continuum-space limit. *Phys. Rev. A* **103**, 032221 (2021).
51. Tumulka, R. Absorbing boundary condition as limiting case of imaginary potentials. *Commun. Theor. Phys.* <https://doi.org/10.48550/arXiv.1911.12730> (2022).
52. Jurić, T. & Nikolić, H. Arrival time from the general theory of quantum time distributions. *Eur. Phys. J. Plus* **137**, 1–13 (2022).
53. Jurman, D. & Nikolić, H. The time distribution of quantum events. *Phys. Lett. A* **396**, 127247 (2021).
54. Jurić, T. & Nikolić, H. Passive quantum measurement: arrival time, quantum zeno effect and gambler’s fallacy. *arXiv* <https://doi.org/10.48550/arXiv.2207.09140> (2022).
55. Roncallo, S., Sacha, K. & Maccone, L. When does a particle arrive? *Quantum* **7**, 968 (2023).
56. Damborenea, J. A., Egusquiza, I. L., Hegerfeldt, G. C. & Muga, J. G. Measurement-based approach to quantum arrival times. *Phys. Rev. A* **66**, 052104 (2002).
57. Muga, J., Brouard, S. & Macias, D. Time of arrival in quantum mechanics. *Ann. Phys.* **240**, 351–366 (1995).
58. Halliwell, J. J. Path-integral analysis of arrival times with a complex potential. *Phys. Rev. A* **77**, 062103 (2008).
59. Andrews, M. et al. Observation of interference between two bose condensates. *Science* **275**, 637–641 (1997).
60. Shin, Y. et al. Atom interferometry with bose-einstein condensates in a double-well potential. *Phys. Rev. Lett.* **92**, 050405 (2004).
61. Cronin, A. D., Schmiedmayer, J. & Pritchard, D. E. Optics and interferometry with atoms and molecules. *Rev. Mod. Phys.* **81**, 1051–1129 (2009).
62. Keller, M. et al. Bose-einstein condensate of metastable helium for quantum correlation experiments. *Phys. Rev. A* **90**, 063607 (2014).
63. Khakimov, R. I. et al. Ghost imaging with atoms. *Nature* **540**, 100–103 (2016).
64. Kurtstiefer, C. & Mlynek, J. A 2-dimensional detector with high spatial and temporal resolution for metastable rare gas atoms. *Appl. Phys. B* **64**, 85–90 (1996).
65. Hall, M. J. W., Deckert, D.-A. & Wiseman, H. M. Quantum phenomena modeled by interactions between many classical worlds. *Phys. Rev. X* **4**, 041013 (2014).
66. Viale, A., Vicari, M. & Zanghi, N. Analysis of the loss of coherence in interferometry with macromolecules. *Phys. Rev. A* **68**, 063610 (2003).
67. Paul, T. & Qureshi, T. Measuring quantum coherence in multislit interference. *Phys. Rev. A* **95**, 042110 (2017).
68. Mishra, S., Venugopalan, A. & Qureshi, T. Decoherence and visibility enhancement in multipath interference. *Phys. Rev. A* **100**, 042122 (2019).
69. Fang, A.-p., Chen, Y.-l., Li, F.-l., Li, H.-r. & Zhang, P. Generation of two-mode gaussian-type entangled states of light via a quantum beat laser. *Phys. Rev. A* **81**, 012323 (2010).
70. Laurat, J. et al. Entanglement of two-mode Gaussian states: characterization and experimental production and manipulation. *J. Opt. B: Quantum Semiclass. Opt.* **7**, S577 (2005).
71. Barnea, A. R., Cheshnovsky, O. & Even, U. Matter-wave diffraction approaching limits predicted by feynman path integrals for multipath interference. *Phys. Rev. A* **97**, 023601 (2018).
72. Vassen, W. et al. Cold and trapped metastable noble gases. *Rev. Mod. Phys.* **84**, 175–210 (2012).
73. Grot, N., Rovelli, C. & Tate, R. S. Time of arrival in quantum mechanics. *Phys. Rev. A* **54**, 4676–4690 (1996).
74. Flores, P. C. M. & Galapon, E. A. Quantum free-fall motion and quantum violation of the weak equivalence principle. *Phys. Rev. A* **99**, 042113 (2019).
75. Aharonov, Y. et al. Finally making sense of the double-slit experiment. *Proc. Natl Acad. Sci. USA* **114**, 6480–6485 (2017).
76. Galapon, E. A. Theory of quantum arrival and spatial wave function collapse on the appearance of particle. *Proc. R. Soc. A: Math. Phys. Eng. Sci.* **465**, 71–86 (2009).
77. Pandey, S. et al. Hypersonic bose-einstein condensates in accelerator rings. *Nature* **570**, 205–209 (2019).
78. Anastopoulos, C. & Savvidou, N. Time-of-arrival correlations. *Phys. Rev. A* **95**, 032105 (2017).
79. Hegerfeldt, G. C. Violation of causality in relativistic quantum theory? *Phys. Rev. Lett.* **54**, 2395–2398 (1985).
80. Sebens, C. T. Electromagnetism as quantum physics. *Found. Phys.* **49**, 365–389 (2019).
81. Kazemi, M. J., Hashamipour, H. & Barati, M. H. Probability density of relativistic spinless particles. *Phys. Rev. A* **98**, 012125 (2018).
82. Gliserin, A., Walbran, M. & Baum, P. A high-resolution time-of-flight energy analyzer for femtosecond electron pulses at 30 keV. *Rev. Sci. Instrum.* **87**, 033302 (2016).
83. Kurtstiefer, C., Pfau, T., Ekstrom, C. R. & Mlynek, J. Time-resolved detection of atoms diffracted from a standing light wave. *Appl. Phys. B* **60**, 229–232 (1995).

84. Copley, J. R. & Udovic, T. J. Neutron time-of-flight spectroscopy. *J. Res. Natl. Inst. Stand. Technol.* **98**, 71 (1993).
85. Kothe, A. et al. Time-of-flight electron spectrometer for a broad range of kinetic energies. *Rev. Sci. Instr.* **84**, 023106 (2013).
86. Vona, N. & Dürr, D. in *The Role of the Probability Current for Time Measurements*, 95–112 (Springer Berlin Heidelberg, Berlin, Heidelberg, 2015).
87. Arce, J. C. Unification of the conditional probability and semiclassical interpretations for the problem of time in quantum theory. *Phys. Rev. A* **85**, 042108 (2012).
88. Aharonov, Y. & Bohm, D. Time in the quantum theory and the uncertainty relation for time and energy. *Phys. Rev.* **122**, 1649 (1961).
89. Paul, H. Über quantenmechanische zeitoperatoren. *Ann. Phys.* **464**, 252–261 (1962).
90. Muga, J. & Leavens, C. Arrival time in quantum mechanics. *Phys. Rep.* **338**, 353–438 (2000).
91. Giannitrapani, R. Positive-operator-valued time observable in quantum mechanics. *Int. J. Theor. Phys.* **36**, 1575–1584 (1997).
92. Egusquiza, I. L. & Muga, J. G. Free-motion time-of-arrival operator and probability distribution. *Phys. Rev. A* **61**, 012104 (1999).
93. Muga, G., Mayato, R. S. & Egusquiza, I. *Time in Quantum Mechanics* Vol. 734 (Springer Science & Business Media, 2007).
94. Egusquiza, I., Muga, J., Navarro, B. & Ruschhaupt, A. Comment on: “on the standard quantum-mechanical approach to times of arrival”. *Phys. Lett. A* **313**, 498–501 (2003).
95. Leavens, C. Spatial nonlocality of the “standard” arrival-time distribution. *Phys. Lett. A* **338**, 19–27 (2005).
96. Leavens, C. Is the peculiar spatial nonlocality of the “standard” arrival-time distribution an artifact of using a nonrelativistic approach? *Phys. Lett. A* **362**, 256–259 (2007).
97. Galapon, E. A. Shouldn't there be an antithesis to quantization? *J. Math. Phys.* **45**, 3180–3215 (2004).
98. Galapon, E. A., Caballar, R. F. & Bahague Jr, R. T. Confined quantum time of arrivals. *Phys. Rev. Lett.* **93**, 180406 (2004).
99. Galapon, E. A., Delgado, F., Muga, J. G. & Egusquiza, I. N. Transition from discrete to continuous time-of-arrival distribution for a quantum particle. *Phys. Rev. A* **72**, 042107 (2005).
100. Galapon, E. A. Only above barrier energy components contribute to barrier traversal time. *Phys. Rev. Lett.* **108**, 170402 (2012).
101. Galapon, E. A. Self-adjoint time operator is the rule for discrete semi-bounded hamiltonians. *Proc. R. Soc. A: Math. Phys. Eng. Sci.* **458**, 2671–2689 (2002).
102. Dias, E. O. & Parisio, F. Space-time-symmetric extension of nonrelativistic quantum mechanics. *Phys. Rev. A* **95**, 032133 (2017).
103. Halliwell, J. & Yearsley, J. Quantum arrival time formula from decoherent histories. *Phys. Lett. A* **374**, 154–157 (2009).
104. Boonchui, S. & Hutem, A. The arrival-time distribution: the extended probability approaches. *J. Phys. A: Math. Theor.* **46**, 105305 (2013).
105. Hannstein, V., Hegerfeldt, G. C. & Muga, J. G. Quantum optical time-of-arrival model in three dimensions. *J. Phys. B* **38**, 409 (2005).
106. Leavens, C. Arrival time distributions. *Phys. Lett. A* **178**, 27–32 (1993).
107. McKinnon, W. R. & Leavens, C. R. Distributions of delay times and transmission times in bohm's causal interpretation of quantum mechanics. *Phys. Rev. A* **51**, 2748–2757 (1995).
108. Leavens, C. Timing quantum particles from the perspective of bohmian mechanics. *Superlattices Microstruct.* **23**, 795–807 (1998).
109. Ali, M. M., Majumdar, A. S., Home, D. & Sengupta, S. Spin-dependent observable effect for free particles using the arrival time distribution. *Phys. Rev. A* **68**, 042105 (2003).
110. Dürr, D., Goldstein, S. & Zanghi, N. Quantum equilibrium and the origin of absolute uncertainty. *J. Stat. Phys.* **67**, 843–907 (1992).
111. Valentini, A. & Westman, H. Dynamical origin of quantum probabilities. *Proc. R. Soc. A: Math. Phys. Eng. Sci.* **461**, 253–272 (2005).
112. Grübl, G. & Rheinberger, K. Time of arrival from bohmian flow. *J. Phys. A: Math. Gen.* **35**, 2907 (2002).
113. Misra, B. & Sudarshan, E. G. The zeno's paradox in quantum theory. *J. Math. Phys.* **18**, 756–763 (1977).
114. Porras, M. A., Luis, A. & Gonzalo, I. Quantum zeno effect for a free-moving particle. *Phys. Rev. A* **90**, 062131 (2014).
115. Fevens, T. & Jiang, H. Absorbing boundary conditions for the schrödinger equation. *SIAM J. Sci. Comput.* **21**, 255–282 (1999).

Acknowledgements

We sincerely thank S. Goldstein, S. Das, M. Khorrami, L. Maccone, H. M. Wiseman, H. Nikolic, W. Struyve, E. Galapon, K. Sacha, and M. H. Barati for their kindly feedback and helpful comments.

Author contributions

A.A.R. and M.K. conceived the research. A.A.R. performed the calculations and simulations. M.K. reviewed and improved the calculations and simulation results. M.G. and A.B. supervised the study. A.A.R. and M.K. wrote the first draft, discussed the results and physical interpretation, and wrote the final version of the manuscript. All authors reviewed the manuscript.

Competing interests

The authors declare no competing interests.

Additional information

Supplementary information The online version contains supplementary material available at <https://doi.org/10.1038/s42005-023-01315-9>.

Correspondence and requests for materials should be addressed to Ali Ayatollah Rafsanjani.

Peer review information *Communications Physics* thanks the anonymous reviewers for their contribution to the peer review of this work. A peer review file is available.

Reprints and permission information is available at <http://www.nature.com/reprints>

Publisher's note Springer Nature remains neutral with regard to jurisdictional claims in published maps and institutional affiliations.



Open Access This article is licensed under a Creative Commons Attribution 4.0 International License, which permits use, sharing, adaptation, distribution and reproduction in any medium or format, as long as you give appropriate credit to the original author(s) and the source, provide a link to the Creative Commons license, and indicate if changes were made. The images or other third party material in this article are included in the article's Creative Commons license, unless indicated otherwise in a credit line to the material. If material is not included in the article's Creative Commons license and your intended use is not permitted by statutory regulation or exceeds the permitted use, you will need to obtain permission directly from the copyright holder. To view a copy of this license, visit <http://creativecommons.org/licenses/by/4.0/>.

© The Author(s) 2023